LETTER

doi:10.1038/nature12340

Sequential deposition as a route to high-performance perovskite-sensitized solar cells

Julian Burschka[1]*, Norman Pellet[1,2]*, Soo-Jin Moon[1], Robin Humphry-Baker[1], Peng Gao[1], Mohammad K. Nazeeruddin[1] & Michael Grätzel[1]

Following pioneering work[1], solution-processable organic–inorganic hybrid perovskites—such as $CH_3NH_3PbX_3$ (X = Cl, Br, I)—have attracted attention as light-harvesting materials for mesoscopic solar cells[2–15]. So far, the perovskite pigment has been deposited in a single step onto mesoporous metal oxide films using a mixture of PbX_2 and CH_3NH_3X in a common solvent. However, the uncontrolled precipitation of the perovskite produces large morphological variations, resulting in a wide spread of photovoltaic performance in the resulting devices, which hampers the prospects for practical applications. Here we describe a sequential deposition method for the formation of the perovskite pigment within the porous metal oxide film. PbI_2 is first introduced from solution into a nanoporous titanium dioxide film and subsequently transformed into the perovskite by exposing it to a solution of CH_3NH_3I. We find that the conversion occurs within the nanoporous host as soon as the two components come into contact, permitting much better control over the perovskite morphology than is possible with the previously employed route. Using this technique for the fabrication of solid-state mesoscopic solar cells greatly increases the reproducibility of their performance and allows us to achieve a power conversion efficiency of approximately 15 per cent (measured under standard AM1.5G test conditions on solar zenith angle, solar light intensity and cell temperature). This two-step method should provide new opportunities for the fabrication of solution-processed photovoltaic cells with unprecedented power conversion efficiencies and high stability equal to or even greater than those of today's best thin-film photovoltaic devices.

We prepared mesoporous TiO_2 (anatase) films by spin-coating a solution of colloidal anatase particles onto a 30-nm-thick compact TiO_2 underlayer. The underlayer was deposited by aerosol spray pyrolysis on a transparent-conducting-oxide-coated glass substrate acting as the electric front contact of the solar cell. Lead iodide (PbI_2) was then introduced into the TiO_2 nanopores by spin-coating a 462 mg ml^{-1} (~1 M) solution of PbI_2 in *N*,*N*-dimethylformamide (DMF) kept at 70 °C. The use of such a high PbI_2 concentration is critical to obtaining the high loading of the mesoporous TiO_2 films required to fabricate solar cells of the highest performance. Further experimental details are provided in Methods.

Figure 1a presents a cross-sectional scanning electron microscopy (SEM) image of the thus-prepared film. The absence of any PbI_2 crystals protruding from the surface of the mesoporous anatase layer shows that our infiltration method leads to a structure in which the PbI_2 is entirely contained within the nanopores of the TiO_2 film.

Dipping the TiO_2/PbI_2 composite film into a solution of CH_3NH_3I in 2-propanol (10 mg ml^{-1}) changes its colour immediately from yellow to dark brown, indicating the formation of $CH_3NH_3PbI_3$. We monitored the dynamics of the formation of the perovskite by optical absorption, emission and X-ray diffraction (XRD) spectroscopy. Figure 1b shows that the increase over time of the perovskite absorption at 550 nm is

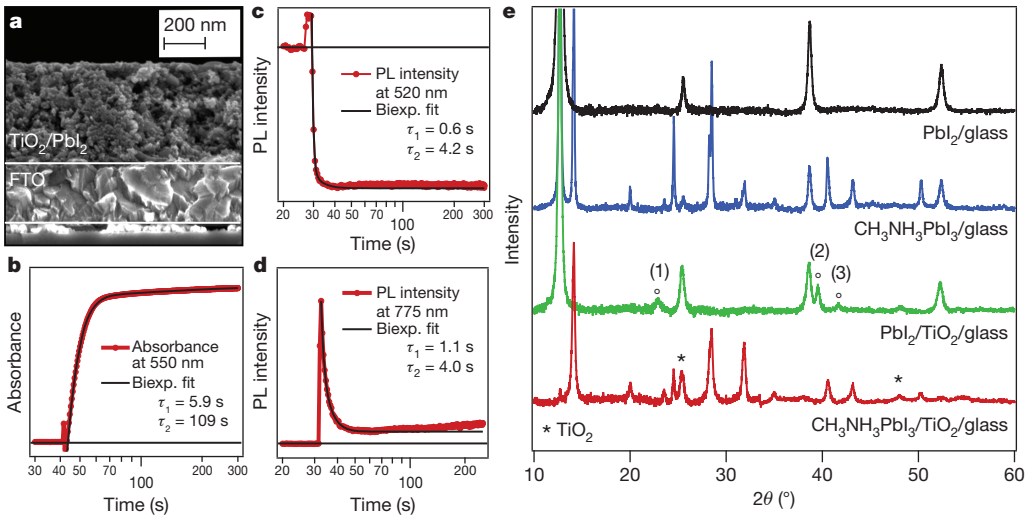

Figure 1 | Transformation of PbI_2 into $CH_3NH_3PbI_3$ within the nanopores of a mesoscopic TiO_2 film. **a**, Cross-sectional SEM of a mesoporous TiO_2 film infiltrated with PbI_2. FTO, fluorine-doped tin oxide. **b**, Change in absorbance at 550 nm of such a film monitored during the transformation. **c**, Change in photoluminescence (PL) intensity at 520 nm monitored during the transformation. Excitation at 460 nm. **d**, Change in photoluminescence intensity at 775 nm monitored during the transformation. Excitation at 660 nm. **e**, X-ray diffraction spectra of PbI_2 on glass and porous TiO_2/glass before and after the transformation. The dipping time was 60 s in both cases. The plot shows the X-ray intensity as a function of 2θ (twice the diffraction angle).

[1]Laboratory of Photonics and Interfaces, Department of Chemistry and Chemical Engineering, Swiss Federal Institute of Technology, Station 6, CH-1015 Lausanne, Switzerland. [2]Max-Planck-Institute for Solid-State Research, Heisenbergstraße 1, D-70569 Stuttgart, Germany.
*These authors contributed equally to this work.

practically complete within a few seconds of exposing the PbI_2-loaded TiO_2 film to the CH_3NH_3I solution. A small additional increase in the absorbance, occurring on a timescale of 100 s and contributing only a few per cent to the total increase of the signal, is attributed to morphological changes producing enhanced light scattering. The conversion is accompanied by a quenching of the PbI_2 emission at 425 nm (Fig. 1c) and a concomitant increase in the perovskite luminescence at 775 nm (Fig. 1d). The latter emission passes through a maximum before decreasing to a stationary value. This decrease results from self-absorption of the luminescence by the perovskite formed during the reaction with CH_3NH_3I. The traces were fitted to a biexponential function yielding the decay times stated in Fig. 1b–d. We note that the increase in the emission intensity before the quenching in Fig. 1c is an optical artefact that results from opening the sample compartment to add the CH_3NH_3I solution.

The green and red curves in Fig. 1e show X-ray powder diffraction spectra measured before and, respectively, after the TiO_2/PbI_2 nanocomposite film is brought into contact with the CH_3NH_3I solution. For comparison, we spin-coated the PbI_2 also on a flat glass substrate and exposed the resulting film to a CH_3NH_3I solution in the same manner as the TiO_2/PbI_2 nanocomposite. On the basis of literature data, the PbI_2 deposited by spin-coating from DMF solution crystallizes in the form of the hexagonal 2H polytype, the most common PbI_2 modification (Inorganic Crystal Structure Database, collection code 68819; http://www.fiz-karlsruhe.com/icsd.html). Moreover, the results show that on a flat glass substrate, crystals grow in a preferential orientation along the *c* axis, hence the appearance of only four diffraction peaks, corresponding to the (001), (002), (003) and (004) lattice planes (Fig. 1e, black curve). For the PbI_2 loaded on a mesoporous TiO_2 film (Fig. 1e, green curve), we find three additional diffraction peaks that do not originate from TiO_2, suggesting that the anatase scaffold induces a different orientation for the PbI_2 crystal growth. The peaks labelled (2) and (3) in Fig. 1e can be attributed to the (110) and (111) lattice planes of the 2H polytype. Peak (1) is assigned to a different PbI_2 variant, whose identification is beyond the scope of this report in view of the large number of polytypes that have been reported for PbI_2 (ref. 16).

During the reaction with CH_3NH_3I, we observe the appearance of a series of new diffraction peaks that are in good agreement with literature data on the tetragonal phase of the $CH_3NH_3PbI_3$ perovskite[17]. However, when PbI_2 is deposited on a flat film (Fig. 1e, blue curve) the conversion to perovskite on exposure to the CH_3NH_3I solution is incomplete; a large amount of unreacted PbI_2 remained even after a dipping time of 45 min. This agrees with the observation that the CH_3NH_3I insertion hardly proceeds beyond the surface of thin PbI_2 films, and that the complete transformation of the crystal structure requires several hours[18]. A caveat associated with such long conversion times is that the perovskite dissolves in the methylammonium iodide solution over longer periods, hampering the transformation.

In striking contrast to the behaviour of thin films of PbI_2 deposited on a flat support, the conversion of PbI_2 nanocrystals in the mesoporous TiO_2 film is practically complete on a timescale of seconds, as is evident from the immediate disappearance of its most intense diffraction peak (the (001) peak) and the concomitant appearance of the XRD reflections for the tetragonal perovskite. When the PbI_2 crystals are contained within the mesoporous TiO_2 scaffold, their size is limited to ~22 nm by the pore size of the host. Notably, we find that confining the PbI_2 crystals to such a small size drastically enhances their rate of conversion to perovskite, which is complete within a few seconds of their coming into contact with the methylammonium iodide solution. However, when deposited on a flat surface, larger PbI_2 crystallites in the size range of 50–200 nm are formed, resulting in incomplete conversion of the PbI_2 on exposure to CH_3NH_3I, as shown by XRD. The SEM images of such a film that are depicted in Supplementary Fig. 1e, f show, however, that the perovskite produced by the sequential deposition technique adopts a morphology similar to that of the PbI_2 precursor. Supplementary Fig. 1 also shows that large crystals of $CH_3NH_3PbI_3$ with a wide range of sizes are formed when the perovskite is deposited in a single step from a solution of CH_3NH_3I and PbI_2 in γ-butyrolactone or DMF.

A key finding of the present work is that the confinement of the PbI_2 within the nanoporous network of the TiO_2 film greatly facilitates its conversion to the perovskite pigment. Moreover, the mesoporous scaffold of the host forces the perovskite to adopt a confined nanomorphology.

The literature contains several examples in which a two-step procedure is used to fabricate nanostructures that are not easily, or not at all, accessible by a direct synthetic route. Ion exchange reactions have, for example, been used to convert dispersed II–V semiconductor nanocrystals into the corresponding III–V analogues while preserving particle size and distribution as well as the initial nanomorphology[19–21]. As reported, the thermodynamic driving force of such a reaction is the difference in bulk lattice energy for the two materials, and the initial crystal lattice serves as a template for the formation of the desired compound. As for PbI_2, the insertion of the organic cation is facilitated through the layered PbI_2 structure, which consists of three spatially repeating planes, I–Pb–I (ref. 16). Numerous literature reports show that strong intralayer chemical bonding, as well as only weak interlayer van der Waals interactions, allows the easy insertion of guest molecules between these layers[22–24]. In our case, the large energy of formation of the hybrid perovskite, combined with the nanoscopic morphology of the PbI_2 precursor, which greatly enhances the reaction kinetics, finally enables the transformation to be completed within seconds.

We used the sequential deposition technique to fabricate mesoscopic solar cells employing the triarylamine derivative 2,2′,7,7′-tetrakis(*N*,*N*-di-*p*-methoxyphenylamine)-9,9′-spirobifluorene (spiro-MeOTAD) (Supplementary Fig. 2) as a hole-transporting material (HTM). We note that, following a recently reported concept[25], we use a Co(III) complex as a p-type dopant for the HTM at a molar doping level of 10% to ensure a sufficient conductivity and low series resistance. Figure 2 shows a cross-sectional SEM picture of a typical device. The mesoporous TiO_2 film had an optimized thickness of around 350 nm and was infiltrated with the perovskite nanocrystals using the above-mentioned two-step procedure. The HTM was subsequently deposited by spin coating. It penetrates into the remaining available pore volume and forms a 100-nm-thick layer on top of the composite structure. A thin gold layer was thermally evaporated under vacuum onto the HTM, forming the back contact of the device.

We measured the current density (*J*)–voltage (*V*) characteristics of the solar cells under simulated air mass 1.5 global (AM1.5G) solar irradiation and in the dark. Figure 3a shows *J*–*V* curves measured at a light intensity of 95.6 mW cm^{-2} for a typical device. From this, we derive values for the short-circuit photocurrent (J_{sc}), the open-circuit voltage (V_{oc}) and the fill factor of, respectively, 17.1 mA cm^{-2}, 992 mV and 0.73, yielding a solar-to-electric power conversion efficiency (PCE) of 12.9% (Table 1). Statistical data on a larger batch of ten photovoltaic devices is shown in Supplementary Table 1. From the

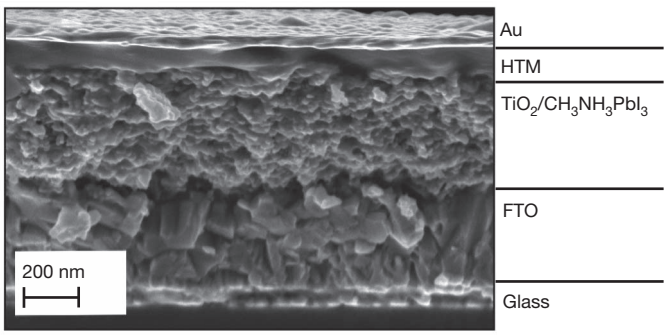

Figure 2 | Cross-sectional SEM of a complete photovoltaic device. Note that the thin TiO_2 compact layer present between the FTO and the mesoscopic composite is not resolved in the SEM image.

average PCE value of 12.0% ± 0.5% and the small standard deviation, we infer that photovoltaics with excellent performance and high reproducibility can be realized using the method reported here.

Figure 3b shows the incident-photon-to-current conversion efficiency (IPCE), or external quantum efficiency, spectrum for the perovskite cell. Generation of photocurrent starts at 800 nm, in agreement with the bandgap of the $CH_3NH_3PbI_3$, and reaches peak values of over 90% in the short-wavelength region of the visible spectrum. Integrating the overlap of the IPCE spectrum with the AM1.5G solar photon flux yields a current density of 18.4 mA cm^{-2}, which is in excellent agreement with the measured photocurrent density, extrapolated to 17.9 mA cm^{-2} at the standard solar AM1.5G intensity of 100 mW cm^{-2}. This confirms that any mismatch between the simulated sunlight and the AM1.5G standard is negligibly small. Comparison with the absorptance or light-harvesting efficiency (LHE) depicted in Fig. 3c reveals that the low IPCE values in the range of 600–800 nm result from the smaller absorption of the perovskite in this spectral region. This is also reflected in the spectrum of the internal quantum efficiency, or absorbed-photon-to-current conversion efficiency (APCE), which can be derived from the IPCE and LHE and is shown in Fig. 3d. The APCE is greater than 90% over the whole visible region, without correction for reflective losses, indicating that the device achieves near-unity quantum yield for the generation and collection of charge carriers.

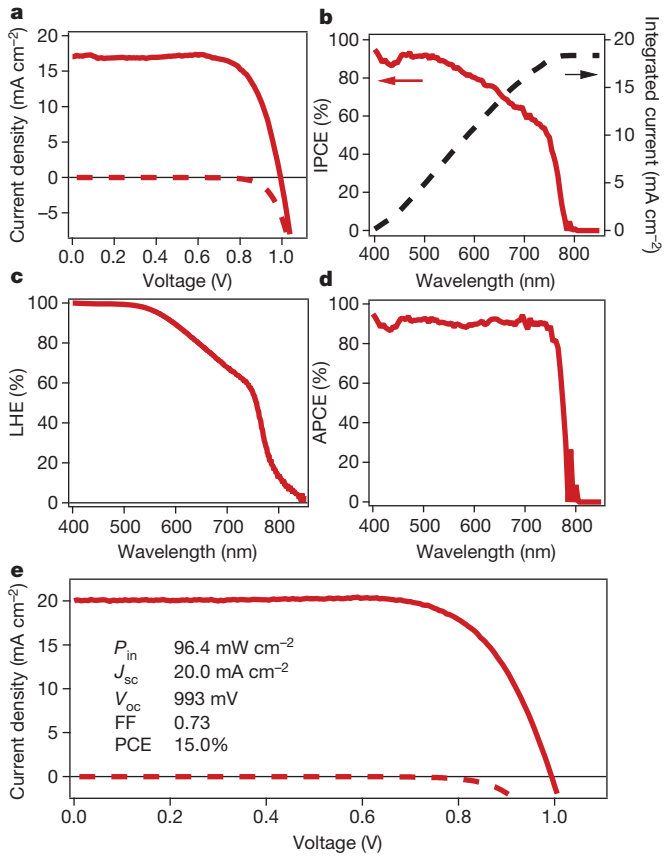

Figure 3 | Photovoltaic device characterization. **a**, *J*–*V* curves for a photovoltaic device measured at a simulated AM1.5G solar irradiation of 95.6 mW cm^{-2} (solid line) and in the dark (dashed line). **b**, IPCE spectrum. The right-hand axis indicates the integrated photocurrent that is expected to be generated under AM1.5G irradiation. **c**, LHE spectrum. **d**, APCE spectrum derived from the IPCE and LHE. **e**, *J*–*V* curves for a best-performing cell measured at a simulated AM1.5G solar irradiation of 96.4 mW cm^{-2} (solid line) and in the dark (dashed line). The device was fabricated using slightly modified deposition conditions (Methods). FF, fill factor.

Table 1 | Photovoltaics performance at different light intensities

Intensity (mW cm^{-2})	J_{sc} (mA cm^{-2})	V_{oc} (mV)	Fill factor	PCE (%)
9.3	1.7	901	0.77	12.6
49.8	8.9	973	0.75	13.0
95.6	17.1	992	0.73	12.9

In an attempt to increase the loading of the perovskite absorber on the TiO_2 structure and to obviate the lack of absorption in the long-wavelength region of the spectrum, we slightly modified the conditions for the deposition of the PbI_2 precursor as well as the transformation reaction. Details are provided in Methods. The *J*–*V* characteristics of the best-performing cell of the series that was fabricated in this manner are depicted in Fig. 3e. From this data, we derive values of 20.0 mA cm^{-2}, 993 mV and 0.73 for J_{sc}, V_{oc} and the fill factor, respectively, yielding a PCE of 15.0% measured at a light intensity of P_{in} = 96.4 mW cm^{-2}. To the best of our knowledge, this is the highest power conversion efficiency reported so far for organic or hybrid inorganic–organic solar cells and one of the highest for any solution-processed photovoltaic device. Several solar cells with PCEs between 14% and 15% were fabricated. One of these devices was sent to an accredited photovoltaic calibration laboratory for certification, confirming a power conversion efficiency of 14.14% measured under standard AM1.5G reporting conditions. Detailed photovoltaics data for this device can be found in Supplementary Fig. 3. Compared with the devices from which we took the data shown in Fig. 3a and Supplementary Table 1, these top-performance devices benefit from a significantly higher photocurrent. We attribute this trend to the increased loading of the porous TiO_2 film with the perovskite pigment and to increased light scattering, improving the long-wavelength response of the cell. The increase in light scattering is likely to result from the additional pre-wetting step that was used for the top-performance devices. The pre-wetting locally decreases the methylammonium iodide concentration, inducing the growth of larger crystals. Detailed studies that aim to identify the key role of the different parameters during the sequential deposition are ongoing.

To test the stability of the perovskite-based photovoltaics prepared using the aforementioned procedure, we subjected a sealed cell to long-term light soaking at a light intensity of ~100 mW cm^{-2} and a temperature of 45 °C. The device was encapsulated under argon and maintained at the optimal electric power output during the ageing using maximum-power-point tracking. We found a very promising long-term stability: the photovoltaic device maintained more than 80% of its initial PCE after a period of 500 h (Supplementary Fig. 4). Also, it is notable that we do not observe any change in the short-circuit photocurrent, indicating that there is no photodegradation of the perovskite light harvester. The decrease in PCE is therefore due only to a decrease in both the open-circuit potential and the fill factor, and the similar shape of the two decays suggests that they are linked to the same degradation mechanism. The change in these two parameters is mainly due to a decrease in the shunt resistance, as is apparent from Supplementary Fig. 5, where *J*–*V* curves of the device before and after the ageing process are shown.

The sequential deposition method for the fabrication of perovskite-sensitized mesoscopic solar cells introduced here provides a means to achieve excellent photovoltaic performance with high reproducibility. The power conversion efficiency of 15% achieved with the best device is amongst the highest for solution-processed photovoltaics and sets a new record for organic or hybrid inorganic–organic solar cells in general. Our findings open new routes for the fabrication of perovskite-based photovoltaic devices, because other preformed metal halide mesostructures may be converted into the desired perovskite by the simple insertion reaction detailed here. On the basis of our results, we believe that this new class of mesoscopic solar cells will find widespread application and will eventually lead to devices that rival conventional silicon-based photovoltaics.

METHODS SUMMARY

Device fabrication. Patterned transparent conducting oxide substrates were coated with a TiO_2 compact layer by aerosol spray pyrolysis. A 350-nm-thick mesoporous TiO_2 layer composed of 20-nm-sized particles was then deposited by spin coating. The mesoporous TiO_2 films were infiltrated with PbI_2 by spin-coating a PbI_2 solution in DMF (462 mg ml^{-1}) that was kept at 70 °C. After drying, the films were dipped in a solution of CH_3NH_3I in 2-propanol (10 mg ml^{-1}) for 20 s and rinsed with 2-propanol. After drying, the HTM was deposited by spin-coating a solution of spiro-MeOTAD, 4-tert-butylpyridine, lithium bis(trifluoromethylsulphonyl)imide and tris(2-(1H-pyrazol-1-yl)-4-tert-butylpyridine)cobalt(III) bis(trifluoromethylsulphonyl)imide in chlorobenzene. Gold (80 nm) was thermally evaporated on top of the device to form the back contact. For the fabrication of the best-performing devices, slightly modified conditions were used. First, PbI_2 was spin-cast for 5 s instead of 90 s and, second, the samples were subjected to a 'pre-wetting' by dipping in 2-propanol for 1–2 s before being dipped in the solution of CH_3NH_3I and 2-propanol. For all measurements, devices were equipped with a 0.285-cm^2 metal aperture to define the active area.

Long-term stability. Devices were sealed in argon and subjected to constant light soaking at approximately 100 mW cm^{-2} using an array of light-emitting diodes. During the testing, the devices were maintained at their maximum power point and a temperature of about 45 °C. Current density/voltage curves were recorded automatically every 2 h.

Optical spectroscopy. Mesoporous TiO_2 films were deposited on microscope glass slides and infiltrated with PbI_2 following the above-mentioned procedure. The samples were then placed vertically in a cuvette with a path length of 10 mm. The solution of CH_3NH_3I was then rapidly injected into the cuvette while either the photoluminescence or the optical transmission was monitored.

Full Methods and any associated references are available in the online version of the paper.

Received 3 April; accepted 29 May 2013.
Published online 10 July 2013.

1. Kojima, A., Teshima, K., Shirai, Y. & Miyasaka, T. Organometal halide perovskites as visible-light sensitizers for photovoltaic cells. *J. Am. Chem. Soc.* **131,** 6050–6051 (2009).
2. Hagfeldt, A., Boschloo, G., Sun, L., Kloo, L. & Pettersson, H. Dye-sensitized solar cells. *Chem. Rev.* **110,** 6595–6663 (2010).
3. Im, J.-H. *et al.* 6.5% efficient perovskite quantum-dot-sensitized solar cell. *Nanoscale* **3,** 4088–4093 (2011).
4. Kim, H.-S. *et al.* Lead iodide perovskite sensitized all-solid-state submicron thin film mesoscopic solar cell with efficiency exceeding 9%. *Sci. Rep.* **2,** 591 (2012).
5. Lee, M. M., Teuscher, J., Miyasaka, T., Murakami, T. N. & Snaith, H. J. Efficient hybrid solar cells based on meso-superstructured organometal halide perovskites. *Science* **338,** 643–647 (2012).
6. Etgar, L. *et al.* Mesoscopic $CH_3NH_3PbI_3/TiO_2$ heterojunction solar cells. *J. Am. Chem. Soc.* **134,** 17396–17399 (2012).
7. Im, J.-H., Chung, J., Kim, S.-J. & Park, N.-G. Synthesis, structure, and photovoltaic property of a nanocrystalline 2H perovskite-type novel sensitizer $(CH_3CH_2NH_3)PbI_3$. *Nanoscale Res. Lett.* **7,** 353 (2012).
8. Edri, E., Kirmayer, S., Cahen, D. & Hodes, G. High open-circuit voltage solar cells based on organic-inorganic lead bromide perovskite. *Phys. Chem. Lett.* **4,** 897–902 (2013).
9. Crossland, E. J. W. *et al.* Mesoporous TiO_2 single crystals delivering enhanced mobility and optoelectronic device performance. *Nature* **495,** 215–219 (2013).
10. Noh, J. H., Im, S. H., Heo, J. H., Mandal, T. N. & Seok, S. I. Chemical management for colorful, efficient, and stable inorganic–organic hybrid nanostructured solar cells. *Nano Lett.* **13,** 1764–1769 (2013).
11. Cai, B., Xing, Y., Yang, Z., Zhang, W.-H. & Qiu, J. High performance hybrid solar cells sensitized by organolead halide perovskites. *Energy Environ. Sci.* **6,** 1480–1485 (2013).
12. Qui, J. *et al.* All-solid-state hybrid solar cells based on a new organometal halide perovskite sensitizer and one-dimensional TiO_2 nanowire arrays. *Nanoscale* **5,** 3245–3248 (2013).
13. Ball, J. M., Lee, M. M., Hey, A. & Snaith, H. J. Low-temperature processed meso-superstructured to thin-film perovskite solar cells. *Energy Environ. Sci.* **6,** 1739–1743 (2013).
14. Bi, D., Yang, L., Boschloo, G., Hagfeldt, A. & Johansson, E. M. J. Effect of different hole transport materials on recombination in $CH_3NH_3PbI_3$ perovskite-sensitized mesoscopic solar cells. *J. Phys. Chem. Lett.* **4,** 1532–1536 (2013).
15. Heo, J. H. *et al.* Efficient inorganic–organic hybrid heterojunction solar cells containing perovskite compound and polymeric hole conductors. *Nature Photon.* **7,** 486–492 (2013).
16. Beckmann, A. A review of polytypism in lead iodide. *Cryst. Res. Technol.* **45,** 455–460 (2010).
17. Baikie, T. *et al.* Synthesis and crystal chemistry of the hybrid perovskite (CH3NH3)PbI3 for solid-state sensitized solar cell applications. *J. Mater. Chem. A* **1,** 5628–5641 (2013).
18. Liang, K., Mitzi, D. B. & Prikas, M. T. Synthesis and characterization of organic-inorganic perovskite thin films prepared using a versatile two-step dipping technique. *Chem. Mater.* **10,** 403–411 (1998).
19. Beberwyck, B. J. & Alivisatos, A. P. Ion exchange synthesis of III–V nanocrystals. *J. Am. Chem. Soc.* **134,** 19977–19980 (2012).
20. Luther, J. M., Zheng, H., Sadtler, B. & Alivisatos, A. P. Synthesis of PbS nanorods and other ionic nanocrystals of complex morphology by sequential cation exchange reactions. *J. Am. Chem. Soc.* **131,** 16851–16857 (2009).
21. Li, H. *et al.* Sequential cation exchange in nanocrystals: preservation of crystal phase and formation of metastable phases. *Nano Lett.* **11,** 4964–4970 (2011).
22. Gurina, G. I. & Savchenko, K. V. Intercalation and formation of complexes in the system of lead(II) iodide–ammonia. *J. Solid State Chem.* **177,** 909–915 (2004).
23. Preda, N., Mihut, L., Baibarac, M., Baltog, I. & Lefrant, S. A distinctive signature in the Raman and photoluminescence spectra of intercalated PbI_2. *J. Phys. Condens. Matter* **18,** 8899–8912 (2006).
24. Warren, R. F. & Liang, W. Y. Raman spectroscopy of new lead iodide intercalation compounds. *J. Phys. Condens. Matter* **5,** 6407–6418 (1993).
25. Burschka, J. *et al.* Tris(2-(1H-pyrazol-1-yl)pyridine)cobalt(III) as p-type dopant for organic semiconductors and its application in highly efficient solid-state dye-sensitized solar cells. *J. Am. Chem. Soc.* **133,** 18042–18045 (2011).

Supplementary Information is available in the online version of the paper.

Acknowledgements We thank M. Marszalek for recording SEM images, M. Tschumi for help with the stability measurements and K. Schenk for the XRD characterization. We acknowledge financial support from Aisin Cosmos R&D Co., Ltd, Japan; the European Community's Seventh Framework Programme (FP7/2007-2013) ENERGY.2012.10.2.1; NANOMATCELL, grant agreement no. 308997; the Global Research Laboratory Program, Korea; the Center for Advanced Molecular Photovoltaics (award no. KUS-C1-015-21) of King Abdullah University of Science and Technology; and Solvay S.A. M.K.N. thanks the World Class University programmes (Photovoltaic Materials, Department of Material Chemistry, Korea University), funded by the Ministry of Education, Science and Technology through the National Research Foundation of Korea (R31-2008-000-10035-0). M.G. thanks the Max Planck Society for a Max Planck Fellowship at the MPI for Solid State Research in Stuttgart, Germany; the King Abdulaziz University, Jeddah and the Nanyang Technolocal University, Singapore for Adjunct Professor appointments; and the European Research Council for an Advanced Research Grant (ARG 247404) funded under the "Mesolight" project.

Author Contributions J.B. developed the basic concept, carried out the spectroscopic characterization, fabricated and characterized photovoltaic devices, and coordinated the project. N.P. fabricated and characterized photovoltaic devices, optimized device performance and fabricated high-performance devices for the certification. S.-J.M. contributed to the fabrication and characterization of photovoltaic devices. R.H.-B. contributed to the spectroscopic characterization and data analysis. P.G. synthesized CH_3NH_3I. M.G. and J.B. analysed the data and wrote the paper. M.K.N. contributed to the supervision of the project. M.G. had the idea for, and directed, the project. All authors reviewed the paper.

Author Information Reprints and permissions information is available at www.nature.com/reprints. The authors declare no competing financial interests. Readers are welcome to comment on the online version of the paper. Correspondence and requests for materials should be addressed to M.G. (michael.graetzel@epfl.ch).

METHODS

Materials. Unless stated otherwise, all materials were purchased from Sigma-Aldrich or Acros Organics and used as received. Spiro-MeOTAD was purchased from Merck KGaA. CH_3NH_3I was synthesized according to a reported procedure[3].

Device fabrication. First, laser-patterned, FTO-coated glass substrates (Tec15, Pilkington) were cleaned by ultrasonication in an alkaline, aqueous washing solution, rinsed with deionized water, ethanol and acetone, and subjected to an O_3/ultraviolet treatment for 30 min. A 20–40-nm-thick TiO_2 compact layer was then deposited on the substrates by aerosol spray pyrolysis at 450 °C using a commercial titanium diisopropoxide bis(acetylacetonate) solution (75% in 2-propanol, Sigma-Aldrich) diluted in ethanol (1:39, volume ratio) as precursor and oxygen as carrier gas. After cooling to room temperature (~25 °C), the substrates were treated in an 0.04 M aqueous solution of $TiCl_4$ for 30 min at 70 °C, rinsed with deionized water and dried at 500 °C for 20 min.

The mesoporous TiO_2 layer composed of 20-nm-sized particles was deposited by spin coating at 5,000 r.p.m. for 30 s using a commercial TiO_2 paste (Dyesol 18NRT, Dyesol) diluted in ethanol (2:7, weight ratio). After drying at 125 °C, the TiO_2 films were gradually heated to 500 °C, baked at this temperature for 15 min and cooled to room temperature. Prior to their use, the films were again dried at 500 °C for 30 min.

PbI_2 was dissolved in *N*,*N*-dimethylformamide at a concentration of 462 mg ml^{-1} (~1 M) under stirring at 70 °C. The solution was kept at 70 °C during the whole procedure. The mesoporous TiO_2 films were then infiltrated with PbI_2 by spin coating at 6,500 r.p.m. for 90 s and dried at 70 °C for 30 min. After cooling to room temperature, the films were dipped in a solution of CH_3NH_3I in 2-propanol (10 mg ml^{-1}) for 20 s, rinsed with 2-propanol and dried at 70 °C for 30 min.

The HTM was then deposited by spin coating at 4,000 r.p.m. for 30 s. The spin-coating formulation was prepared by dissolving 72.3 mg (2,2′,7,7′-tetrakis(*N*,*N*-di-*p*-methoxyphenylamine)-9,9-spirobifluorene) (spiro-MeOTAD), 28.8 µl 4-tert-butylpyridine, 17.5 µl of a stock solution of 520 mg ml^{-1} lithium bis(trifluoromethylsulphonyl)imide in acetonitrile and 29 µl of a stock solution of 300 mg ml^{-1} tris(2-(1H-pyrazol-1-yl)-4-tert-butylpyridine)cobalt(III) bis(trifluoromethylsulphonyl)imide in acetonitrile in 1 ml chlorobenzene.

Finally, 80 nm of gold was thermally evaporated on top of the device to form the back contact. The device fabrication was carried out under controlled atmospheric conditions and a humidity of <1%. For the fabrication of the best-performing devices exhibiting a PCE of 15%, slightly modified conditions were used. First, PbI_2 was spin-cast at 6,500 r.p.m. for 5 s. Second, the samples were subjected to a 'pre-wetting' by dipping in 2-propanol for 1–2 s before being dipped in the solution of CH_3NH_3I and 2-propanol.

Device characterization. Current–voltage characteristics were recorded by applying an external potential bias to the cell while recording the generated photocurrent with a digital source meter (Keithley Model 2400). The light source was a 450-W xenon lamp (Oriel) equipped with a Schott K113 Tempax sunlight filter (Praezisions Glas & Optik GmbH) to match the emission spectrum of the lamp to the AM1.5G standard. Before each measurement, the exact light intensity was determined using a calibrated Si reference diode equipped with an infrared cut-off filter (KG-3, Schott). IPCE spectra were recorded as functions of wavelength under a constant white light bias of approximately 5 mW cm^{-2} supplied by an array of white light-emitting diodes. The excitation beam coming from a 300-W xenon lamp (ILC Technology) was focused through a Gemini-180 double monochromator (Jobin Yvon Ltd) and chopped at approximately 2 Hz. The signal was recorded using a Model SR830 DSP Lock-In Amplifier (Stanford Research Systems). All measurements were conducted using a non-reflective metal aperture of 0.285 cm^2 to define the active area of the device and avoid light scattering through the sides.

Long-term stability. For long-term stability tests, the devices were sealed in argon using a 50-µm-thick hot-melting polymer and a microscope coverslip, and subjected to constant light soaking at approximately 100 mW cm^{-2}. The light source was an array of white light-emitting diodes (LXM3-PW51 4000K, Philips). During the testing, the devices were maintained at their maximum power point using electronic control and at a temperature of about 45 °C. An automatic *J*–*V* measurement at different light intensities (0%, 1%, 10%, 50% and 100% the solar value) was made every 2 h.

Optical spectroscopy. Mesoporous TiO_2 films were deposited on microscope glass slides and infiltrated with PbI_2 following the above-mentioned procedure. The samples were then placed vertically in a standard cuvette of 10-mm path length using a Teflon holder. A solution of CH_3NH_3I in 2-propanol was then rapidly injected into the cuvette while either the photoluminescence or the optical transmission was monitored. Photoluminescence measurements were carried out on a Horiba Jobin Yvon Fluorolog spectrofluorometer. Optical absorption measurements were carried out on a Varian Cary 5 spectrophotometer.

X-ray diffraction measurements. For XRD measurements, flat PbI_2 and TiO_2/PbI_2 nanocomposites were deposited on microscope glass slides using the above-mentioned procedures. X-ray powder diagrams were recorded on an X'Pert MPD PRO from PANalytical equipped with a ceramic tube (Cu anode, $\lambda = 1.54060$ Å), a secondary graphite (002) monochromator and a RTMS X'Celerator detector, and operated in BRAGG-BRENTANO geometry. The samples were mounted without further modification, and the automatic divergence slit and beam mask were adjusted to the dimensions of the thin films. A step size of 0.008 deg was chosen and an acquisition time of up to 7.5 min deg^{-1}. A baseline correction was applied to all X-ray powder diagrams to remove the broad diffraction peak arising from the amorphous glass slide.